

## Original Article

# Altered lipid metabolism and ferroptosis in sodium hydroxide-induced skin burns: a comprehensive rat model-based analysis

Chi Zhong<sup>1,2\*</sup>, Guangyi Wang<sup>2\*</sup>, Jianda Zhou<sup>1</sup>, Yang Liu<sup>1</sup>, Zhelin Li<sup>1</sup>, Jianfei Zhang<sup>3</sup>, Ke Shi<sup>1</sup>, Peiting Li<sup>1</sup>, Xiaohui Qiu<sup>1</sup>, Xianrui Wu<sup>1</sup>, Shuyue Chen<sup>1</sup>, Fuying Li<sup>1</sup>, Zitong Zhao<sup>1</sup>, Geao Liang<sup>1</sup>, Hui Xu<sup>4</sup>, Dan Xu<sup>1</sup>

<sup>1</sup>The Third Xiangya Hospital of Central South University, No. 138, Tongzipo Road, Yuelu District, Changsha 410013, Hunan, China; <sup>2</sup>Burn Institute of PLA, Department of Burn Surgery, The First Affiliated Hospital of Naval Medical University, Research Unit of Key Techniques for Treatment of Burns and Combined Burns and Trauma Injury, Chinese Academy of Medical Sciences, Shanghai 200433, China; <sup>3</sup>The Second Hospital University of South China, No. 35, Jiefang Avenue, Zhengxiang District, Hengyang 421099, Hunan, China; <sup>4</sup>Hunan Provincial Hospital of Integrated Traditional Chinese and Western Medicine (The Affiliated Hospital of Hunan Academy of Traditional Chinese Medicine), No. 58, Lushan Road, Yuelu District, Changsha 410006, Hunan, China. \*Co-first authors.

Received December 6, 2024; Accepted April 16, 2025; Epub April 25, 2025; Published April 30, 2025

**Abstract:** Objectives: Sodium hydroxide (NaOH) is known to cause severe injuries through lipid saponification; however, the mechanisms underlying NaOH-induced skin injuries, particularly their effects on lipid metabolism and ferroptosis, are unclear. Here, we aimed to elucidate these mechanisms based on lipid profile evaluations and ferroptosis occurrence. Methods: We used experimental rat models of NaOH-induced skin burns (skin exposed to 0.05% NaOH for 90 or 180 s) alongside a sham-treated control group. Skin morphology and integrity were assessed. Differentially expressed lipid profiles were monitored via untargeted lipidomics. Oxidative stress, lipid peroxidation, and iron metabolism were also assessed. The expression of ferroptosis-associated genes, including acyl-CoA synthetase long-chain family member 4 (*ACSL4*), lysophosphatidylcholine acyltransferase 3 (*LPCAT3*), and glutathione peroxidase 4 (*GPX4*), was analysed using immunohistochemical and quantitative reverse transcription-polymerase chain reaction analyses. Results: NaOH exposure for 90 and 180 s caused second- and third-degree burns, respectively, leading to elevated and reduced levels of polyunsaturated and monosaturated fatty acid phospholipids, respectively. Both groups showed significant increases in reactive oxygen species, ferrous iron, and malondialdehyde levels and significant decreases in glutathione levels. *ACSL4* and *LPCAT3* expression increased, and *GPX4* expression decreased. Conclusion: NaOH-induced skin burns disrupt skin appendages, resulting in lipid metabolism alterations and ferroptosis induction. These findings could provide valuable insights for elucidating the precise mechanisms underlying ferroptosis in the context of NaOH burns and for identifying potential therapeutic strategies.

**Keywords:** Ferroptosis, lipid saponification, NaOH burn, skin burn

## Introduction

Although burns attributable to sodium hydroxide (NaOH) represent only 6.5% of reported chemical burns [1], the burns can cause substantial damage to the skin and are more severe than typical burns or burns inflicted by strong acids, leading to considerable discomfort [2, 3]. NaOH reacts with proteins and lipids and causes tissue liquefaction and saponification, which give the injured skin a characteristic 'greasy' or 'soapy' appearance [4].

Lipids supply energy for cellular metabolism and contribute to the molecular framework of cells. As numerous major diseases are associated with abnormal lipid metabolism, changes in lipid composition, metabolism, and metabolising enzyme levels during the onset of diseases have been extensively investigated [5, 6]. However, the traditional methods used for detecting lipids are complex and cumbersome and are often limited to a single or a few lipid classes without offering a comprehensive analysis. Lipidomics has emerged as a methodologi-

cal approach that can be used to systematically examine the roles of lipid molecules within their broader pathways and networks [7]. Similar to proteomics, lipidomics aims to directly analyse the phenotypes of biological activity based on big data, which can contribute to providing a holistic perspective of disease onset, thereby enhancing the early detection, prevention, and management of diseases [8].

Ferroptosis, named for its dependence on iron ions, was formally recognised in 2012 and is distinct from traditional forms of cell necrosis and apoptosis [9]. Morphologically, ferroptotic cells are characterised by reduced or no mitochondrial cristae and diminished mitochondrial volume, whereas the cytoplasmic membrane remains intact, and the nucleus appears normal. Biochemically, ferroptosis involves iron accumulation, glutathione (GSH) deficiency, and lipid peroxidation, with the latter considered pivotal to the process [10-12]. Ferroptosis has been demonstrated to play a key role in a range of diseases and has implications for tumour prevention and treatment [13].

In clinical practice, the texture of NaOH burns [4] can obscure injury boundaries and depth, thereby resulting in potentially substantial patient harm and presenting challenges for surgeons and specialists in burn care units [3, 14]. Although chemical burns rank second after thermal injuries in terms of prevalence, they constitute only a small proportion of total burn cases, with NaOH burns being particularly rare [15]. Previous research on NaOH-induced injuries has predominantly focused on corneal damage, with limited investigations into skin wounds [2, 3]. Given the importance of skin integrity, further research is urgently needed to address this deficiency.

The present study was conducted to address the clinical challenges associated with NaOH-induced skin burns. We hypothesised that by disrupting lipid metabolism, such burns can induce ferroptosis. Consequently, we aimed to assess the morphological and pathological changes in skin burns, focusing specifically on the damage caused to lipid-related structures, using a rat model of NaOH-induced skin burns. To confirm the occurrence of ferroptosis, we performed lipidomic differential analysis to identify specific alterations in lipid content and assess biochemical indicators and key genes.

### Materials and methods

#### *NaOH burn model*

Male Sprague-Dawley (SD) rats (Yuanhe Biotechnology Corporation, Hunan, China), aged 7-8 weeks, were housed in a controlled environment under a 12 h:12 h light/dark cycle and provided with unrestricted access to food and water. The study was approved by the Animal Ethics Committee of Central South University (CSU-2023-0535), and all protocols and procedures were performed in strict adherence to animal care principles. The mid- to lower dorsa of rats were shaved, exposing a skin area adequate to accommodate a 4 × 4 cm square filter paper. The rats were randomly assigned to three groups, namely, the sham, 90 s model, and 180 s model groups, with each group containing three animals. Under isoflurane gas anaesthesia (isoflurane concentration for anaesthesia induction: 3-3.5%; anaesthesia maintenance: 2-2.5%; oxygen flow: 1 L/min), the sham group rats were treated with filter paper soaked in saline, whereas rats in the 90 and 180 s model groups were treated with filter paper soaked in 5% NaOH for 90 and 180 s, respectively. After the experiments, the rats were placed into a euthanasia box, and 20% CO<sub>2</sub> was instilled into the box at a rate of 5.8 L/min, until the rats were no longer moving or breathing, and their pupils were dilated. They were then observed for a further 2-3 min to ensure that they were dead.

#### *Lipidomic analysis*

Chromatographic separation was achieved using a UHPLC Nexera LC-30A system (Shimadzu Corporation, Kyoto, Japan) equipped with a C18 column operated at 45°C. As mobile phases A and B, we used 4:6 water:acetonitrile and 9:1 isopropanol:acetonitrile, respectively, with the following gradient profile: 30% B for 0 to 2 min, increased linearly from 30% to 100% B over 2 to 25 min, and returned to 30% B from 25 to 35 min. High-resolution detection was achieved using a Q Exactive Plus mass spectrometer (Thermo Fisher Scientific, Boston, MA, USA) with an electrospray ionisation source. Mass spectrometry (MS) detection was performed in both the negative and positive ion modes within the mass-to-charge ratio (m/z) range of 200-1800.

## Altered lipid metabolism in NaOH-induced skin burns

**Table 1.** Sequences of the primers used in this study

Gene		Sequence
ACSL4	Forward	5'-CCGCTTGTGACTTTATATGCTACCC-3'
	Reverse	5'-GCCGCCTTCAGTTTGCTTTCC-3'
LPCAT3	Forward	5'-CGCTGGCTTCTCCTACTTCTATGG-3'
	Reverse	5'-GCTGTTTGGCATCTTTCTGGTAC-3'
GPX4	Forward	5'-ACCAGTTCGGGAGGCAGGAG-3'
	Reverse	5'-CACAGTGGGTGGGCATCGTC-3'
$\beta$ -actin	Forward	5'-GGAGTCTACTGGCGTCTTAC-3'
	Reverse	5'-ATGAGCCCTCCACGATGC-3'

A data matrix was generated by extracting and transforming the raw data, which mainly included information such as  $m/z$ , retention time (Rt), and peak area (intensity). Variables in the tables with a relative standard deviation of  $\geq 30\%$  were excluded to minimise the signal interference caused by random errors. The resulting Excel files were imported into LipidSearch software for multivariate mathematical and statistical analyses. Subsequently, differential variables were selected based on the variable importance in projection (VIP) index and Mann-Whitney test analysis. Variables with  $VIP > 1$  and  $P$ -value  $< 0.05$  were regarded as significantly different variables.

### Biochemical analysis

Skin tissue samples were resected from the rats in each group and mixed with 0.9% saline at a 1:9 ratio. For each sample, we obtained a 10% homogenate via mechanical homogenisation in an ice water bath, followed by centrifugation at 2500-3000 rpm for 10 min at 4°C. The resulting supernatant was collected and used to quantify reactive oxygen species (ROS), ferrous ion ( $Fe^{2+}$ ), GSH, and malondialdehyde (MDA) levels using the relevant assay kits (Proteintech, Rosemont, IL, USA).

### Histological analysis

Samples were fixed in 4% paraformaldehyde, embedded in paraffin, and cut into 5- $\mu$ m sections for haematoxylin and eosin staining. Following de-paraffinisation and rehydration, the sections were blocked and incubated overnight at 4°C with the following primary antibodies: anti-ACSL4 (1:50; Aifang Technology, Changsha, China), anti-LPCAT3 (1:200; Aifang Technology), and anti-GPX4 (1:200; Aifang Technology). Following subsequent incubation

with biotinylated goat anti-rabbit IgG antibody (Proteintech) for 30 min at 22°C, the samples were further incubated with a diaminobenzidine reagent (Solarbio Science and Technology, Beijing, China) for 10 min at 37°C. The specimens were thereafter counterstained using haematoxylin (Beyotime, Rosemont, IL, USA) and photographed under a microscope (Motic, Hong

Kong, China), and the average optical density was calculated using ImageJ software (NIH, USA).

### Quantitative reverse transcription-polymerase chain reaction analysis

Total cellular RNA was extracted using TRIzol Reagent (Invitrogen, Carlsbad, CA, USA), according to the manufacturer's instructions. Reverse transcription was performed using a kit from TaKaRa (Otsu, Japan), and subsequent quantitative reverse transcription-polymerase chain reactions (qRT-PCR) was performed using a QuantiTect SYBR Green PCR Kit and an Applied Biosystems QuantStudio 1 thermocycler (Thermo Fisher Scientific). Relative quantification was conducted using the  $2^{-\Delta\Delta Ct}$  method [16], with  $\beta$ -actin mRNA used as the standard for normalising the relative expression of the mRNA of each gene. The sequences of the specific primers used in this study are listed in **Table 1**.

### Statistical analysis

All experimental results were analysed using Prism 9.1.12 (GraphPad, USA), and bar graphs were generated for visual representation. The significance of differences between groups was determined using the Bonferroni correction, following ANOVA for pairwise comparisons. Results with a  $P$ -value  $< 0.05$  were considered statistically significant.

## Results

### Morphological evaluation of the effects of NaOH on skin tissue

To establish a foundation for subsequent experiments, we focused on examining the morphological changes in NaOH-exposed skin tissue.

## Altered lipid metabolism in NaOH-induced skin burns

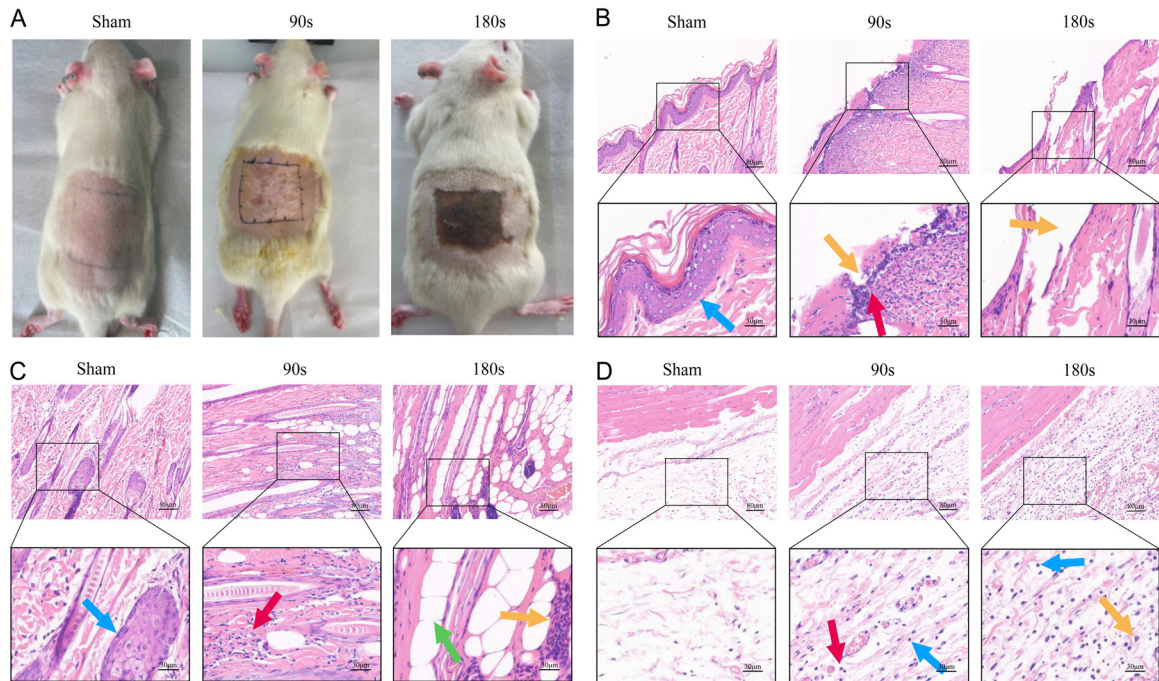


**Figure 1.** Comparison of macroscopic and microscopic views of rat skin wounds. (A) Rat skin wounds in the 90 and 180 s model groups exhibiting characteristics of second- and third-degree burns, respectively. Tissue sections were stained with haematoxylin and eosin. (B) Superficial epidermal and dermal layers: blue arrow, intact epidermal structures; yellow arrows, damaged epidermal structures; red arrow, immune cell infiltration. (C) Deep dermal layers: blue arrow, sebaceous gland; red arrow, immune cell infiltration; green arrow, 'paving stone-like' changes; yellow arrow, necrosis. (D) Subcutaneous tissues: red arrow, plasma cell; blue arrows, lymphocytes; yellow arrow, neutrophil. Magnification (A-D)  $\times 200$ .

In the preliminary experiments, no significant differences were observed in wounds 24 h post-injury compared with the state at the time of injury. The 24-h post-injury time point was selected for further analysis, as the dorsal skin of each group exhibited distinct characteristics at this time point.

Among rats in the sham group (**Figure 1A**), the treated skin was characterised by normal hair growth without exudation. In contrast, the skin of rats in the 90 s model group was pale and moist with scattered translucent bases, indicative of second-degree burns, whereas rats in the 180 s model group had wounds that were dry with carbonised eschar formation and leather-like alterations, consistent with third-degree burns.

Microscopic examination of wound morphology revealed continuous keratin and a well-structured epidermis in the skin tissues of the sham group (**Figure 1B**), whereas in the 90 s model group, the skin was characterised by disrupted keratin and epidermal structures. The rats in

the 180 s model group exhibited epidermal detachment with residual epidermal cells.

Examination of the deep dermis (**Figure 1C**) revealed regularly arranged collagen fibres without hyperplasia in the sham group, with intact sebaceous glands adjacent to hair follicles. Contrastingly, the skin of the 90 s model rats was characterised by swollen collagen fibres and residual sebaceous glands, and that of the 180 s model rats exhibited broken collagen fibres, atrophied outer root sheath cells, and thrombosis of the dermal blood vessels.

Examination of the changes in subcutaneous tissues (**Figure 1D**) revealed a serrated adipose layer and a clear striated muscle fibre margin without inflammatory exudates in the sham group rats. In contrast, in the 90 s model rats, the serrated appearance of the adipose layer was lost, and oedematous muscle fibres and immune cell infiltration were observed. The 180 s model rats exhibited increased fat vacuoles, loss of adipose layer serration, and indistinct muscle cell margins.

# Altered lipid metabolism in NaOH-induced skin burns

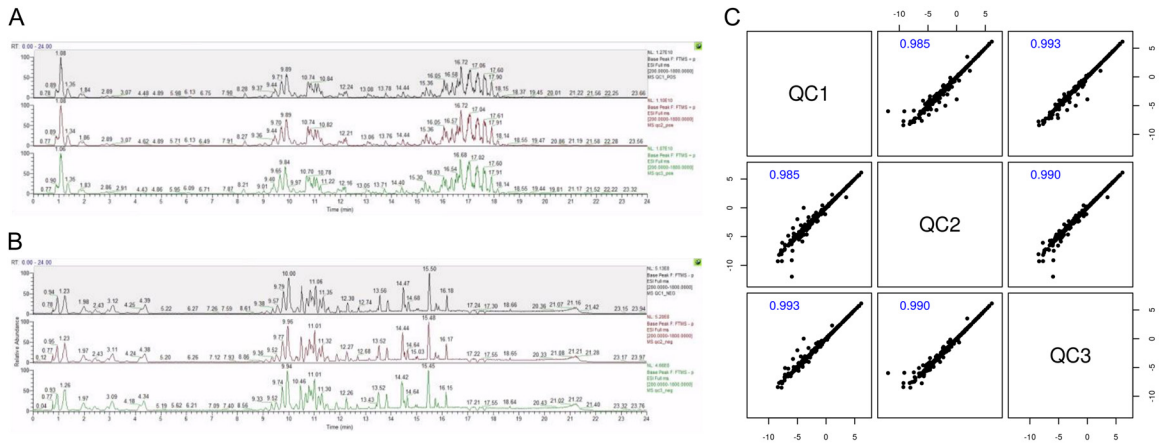


**Figure 2.** Quality control of UHPLC-QTOF/MS. (A, B) Quality control (QC) base peak chromatograms in positive (A) and negative (B) ion modes. (C) Pearson correlation analysis of QC samples.

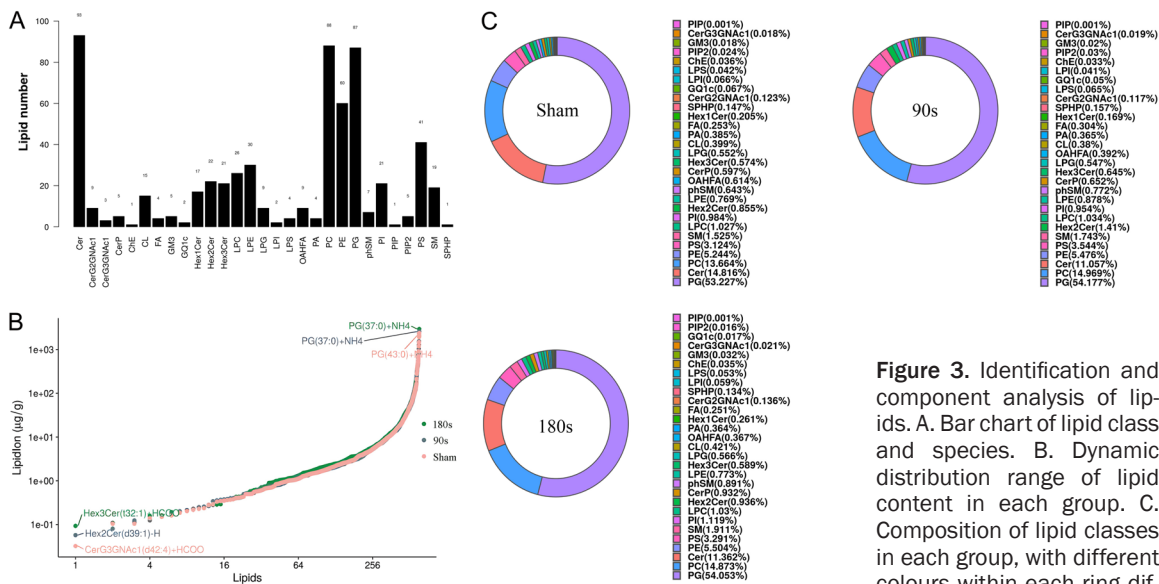


**Figure 3.** Identification and component analysis of lipids. A. Bar chart of lipid class and species. B. Dynamic distribution range of lipid content in each group. C. Composition of lipid classes in each group, with different colours within each ring differentiating the lipid class.

## Quality control of UHPLC-QTOF/MS

Microscopic analysis revealed significant NaOH-induced changes in fat-related appendages within the skin tissues. Consequently, ultra-high-performance liquid chromatography coupled with quadrupole time-of-flight mass spectrometry (UHPLC-QTOF/MS) was employed to further investigate the changes in the lipid profiles. In both positive and negative ion modes (Figure 2A, 2B), the quality control base peak chromatograms revealed an overlap in ion intensity and retention time across the quality control samples. Pearson correlation coefficients among these samples exceeded 0.9,

thereby indicating excellent repeatability and stability (Figure 2C).

## Identification and component analysis of lipids

We identified 29 lipid subclasses and 611 types of lipid molecules using UHPLC-QTOF/MS (Figure 3A). The ranges of the lipid molecule content and composition among the three groups were also analysed (Figure 3B, 3C).

## Differential metabolite profile analysis

Differences between the treatment and sham groups with respect to the contents of different lipid classes are illustrated in Figure 4A, 4B,

## Altered lipid metabolism in NaOH-induced skin burns

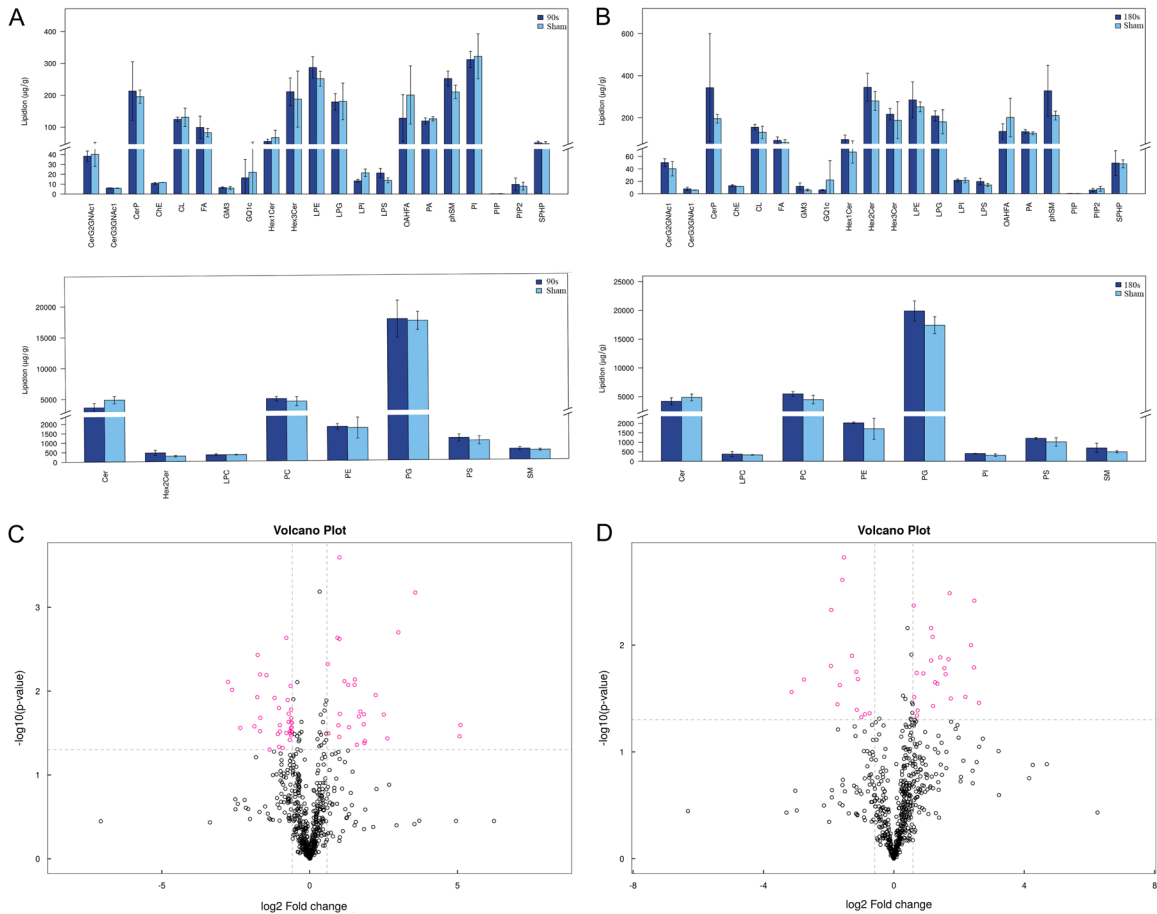


**Figure 4.** Differences in the content of lipid classes and identification of key differentially expressed lipids using univariate analysis. (A, B) Bar charts showing differences in lipid class content: (A) 90 s model group vs. sham group and (B) 180 s model group vs. sham group. (C, D) Volcano plots based on univariate analysis: (C) 90 s model group vs. sham group and (D) 180 s model group vs. sham group. Red points in the volcano plots indicate differentially expressed lipids.

and lipid molecules identified based on univariate analysis are shown in **Figure 4C, 4D**.

Multivariate analysis was employed to identify key differentially expressed lipids among all groups. We subjected the orthogonal projections to latent structures discriminant analysis model to permutation testing (**Figure 5A, 5B**), which successfully distinguished the 90 and 180 s model groups from the sham group (**Figure 5C, 5D**). Compared with those in rats in the sham group, there were 20 and 12 differentially expressed lipids in rats in the 90 and 180 s model groups, respectively (**Tables 2, 3**). These differentially expressed metabolites are summarised in **Figure 5E, 5F**. The primary lipid classes showing differential patterns in the 90 s model and sham groups included sphingomyelin (SM), phytosphingosine (phSM), phosphatidylglycerol (PG), phosphatidylethanolamine (PE), phosphatidylcholine (PC), lysophosphatidylcholine (LPC), ceramide phosphate (CerP), and ceramide (Cer), whereas those differing between the 180 s model and sham groups included PG, PC, lysophosphatidylglycerol (LPG), dihexosylceramide (Hex2Cer), and Cer.

Based on the hierarchical clustering analysis, we constructed heat maps to illustrate differential levels of lipid expression (**Figure 5G, 5H**). In the 90 s model group, significant increases were detected in the levels of SM (d34:1), SM (d42:3), phSM (t36:1), PC (18:0\_18:2), PG (40:1), PC (16:0e\_20:4), PC (20:1e\_14:0), PC (16:0e\_16:0), LPC (32:0), and PC (16:0e\_18:2), whereas decreases were observed in the levels of PC (16:0\_16:1), CerP (t40:2+0), PC (16:1\_16:1), PE (34:2), PE (16:0\_18:1), Cer (t42:1+0), Cer (d41:1), Cer (d34:1+0), Cer

## Altered lipid metabolism in NaOH-induced skin burns

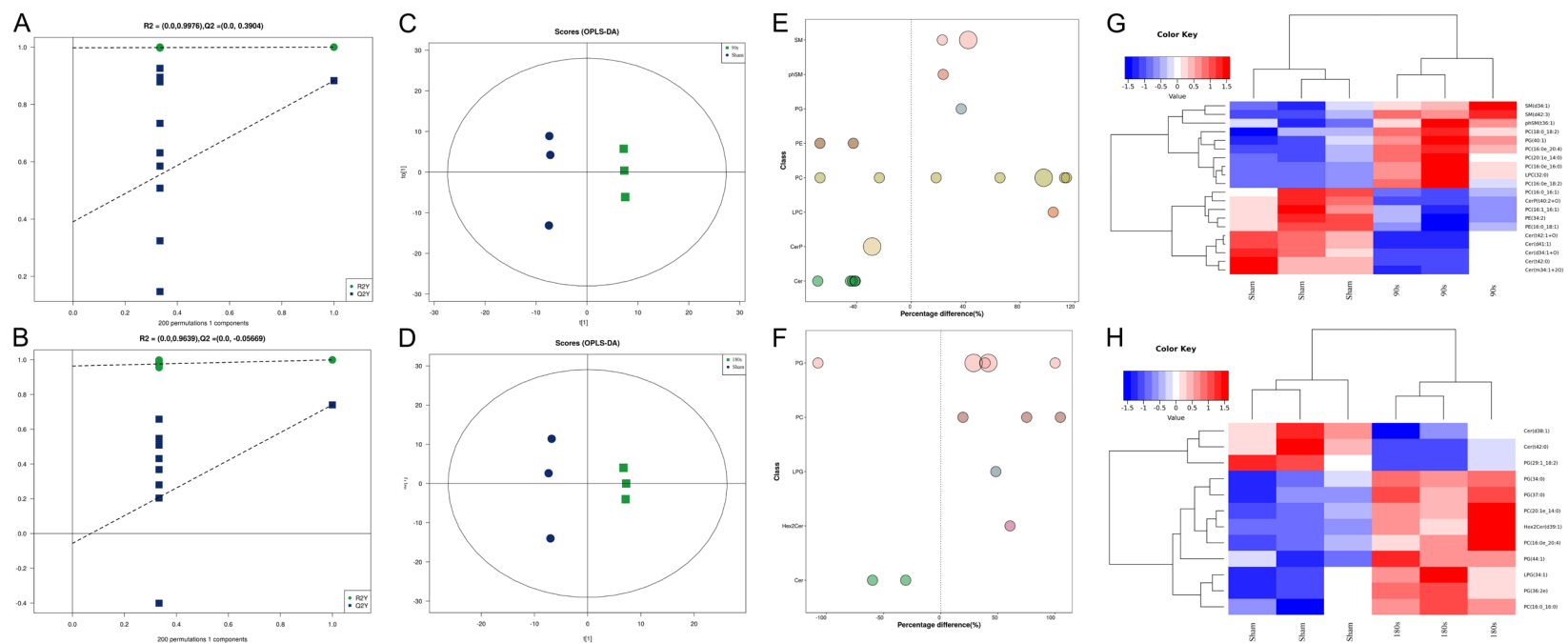


**Figure 5.** Identification of differentially expressed lipids using multivariate analysis. (A, B) Permutation tests on orthogonal projections to latent structures discriminant analysis (OPLS-DA) model: (A) 90 s model group vs. sham group and (B) 180 s model group vs. sham group. (C, D) OPLS-DA score charts: (C) 90 s model group vs. sham group and (D) 180 s model group vs. sham group. (E, F) Bubble charts: (E) 90 s model group vs. sham group and (F) 180 s model group vs. sham group. (G, H) Clustered heat maps: (G) 90 s model group vs. sham group and (H) 180 s model group vs. sham group. Red blocks indicate high lipid expression, whereas blue blocks denote low lipid expression.

## Altered lipid metabolism in NaOH-induced skin burns

**Table 2.** Differentially expressed lipids (90 s model group vs. sham group)

Lipid Ion	Class	Rt (min)	p-value	VIP
Cer (t42:0)+HCOO	Cer	15	0.046224277	1.954983887
Cer (t42:1+0)-H	Cer	15.027	0.026997339	1.390555642
Cer (d34:1+0)+HCOO	Cer	10.437836	0.029823425	4.079598457
Cer (d41:1)+HCOO	Cer	15.052	0.023903005	1.378080166
Cer (m34:1+20)+HCOO	Cer	10.501	0.027725717	2.224750207
CerP (t40:2+0)+HCOO	CerP	9.733	0.007821324	1.929052686
LPC (32:0)+HCOO	LPC	11.592	0.020057999	1.046224849
PC (16:0e_16:0)+HCOO	PC	11.60909992	0.018930091	1.762325824
PC (16:0_16:1)+HCOO	PC	9.714386949	0.03195169	1.654939042
PC (16:1_16:1)-CH3	PC	10.15142864	0.030413182	1.076500123
PC (20:1e_14:0)+HCOO	PC	11.65570861	0.025601251	1.393411878
PC (16:0e_18:2)+HCOO	PC	10.74781713	0.039447582	1.264889094
PC (18:0_18:2)+HCOO	PC	11.17336854	0.03740992	2.345953231
PC (16:0e_20:4)+HCOO	PC	10.53125347	0.007263116	1.959330547
PE (16:0_18:1)-H	PE	11.2667001	0.016577854	1.621650673
PE (34:2)-H	PE	10.15593415	0.025500646	1.076770111
PG (40:1)+H	PG	15.5778927	0.014447777	2.630595665
phSM (t36:1)-CH3	phSM	9.510822921	0.031048181	1.94700059
SM (d34:1)+HCOO	SM	9.533980592	0.045498875	1.797460262
SM (d42:3)+HCOO	SM	12.16995617	0.004754097	1.335619152

Rt, retention time; VIP, variable importance in projection; PG, phosphatidylglycerol; PE, phosphatidylethanolamine; PC, phosphatidylcholine; LPC, lysophosphatidylcholine; CerP, ceramide phosphate; Cer, ceramide; LPG, lysophosphatidylglycerol; SM, sphingomyelin; phSM, phytosphingosine.

**Table 3.** Differentially expressed lipids (180 s model group vs. sham group)

Lipid Ion	Class	Rt (min)	p-value	VIP
Cer (t42:0)+HCOO	Cer	15	0.044440691	2.141100444
Cer (d38:1)+HCOO	Cer	13.44370432	0.048762086	1.876005854
Hex2Cer (d39:1)-H	Hex2Cer	17.43169392	0.018416665	1.233948292
LPG (34:1)+NH4	LPG	11.411	0.045629958	2.021091673
PC (16:0_16:0)+HCOO	PC	10.81110611	0.029738757	1.897272506
PC (20:1e_14:0)+HCOO	PC	11.65570861	0.013904461	1.498590401
PC (16:0e_20:4)+HCOO	PC	10.53125347	0.013570113	2.022577822
PG (34:0)+NH4	PG	11.238	0.006917554	3.527771464
PG (36:2e)+NH4	PG	11.505	0.043045046	1.002916653
PG (37:0)+NH4	PG	10.919	0.004254209	9.13158506
PG (44:1)+Na	PG	15.53198528	0.018720124	1.048982535
PG (29:1_18:2)+H	PG	16.53344648	0.035805427	1.184617036

Rt, retention time; VIP, variable importance in projection; PG, phosphatidylglycerol; PC, phosphatidylcholine; Cer, ceramide; LPG, lysophosphatidylglycerol; Hex2Cer, dihexosylceramide.

(t42:0), and Cer (m34:1+20). In the 180 s model group, we observed significant increases in the levels of PG (34:0), PG (37:0), PC (20:1e\_14:0), Hex2Cer (d39:1), PC (16:0e\_20:4), PG (44:1), LPG (34:1), and PG (36:2e), whereas decreases were observed in the levels of Cer (d38:1), Cer (t42:0), and PG (29:1\_18:2).

### *Immunohistochemical analysis of ferroptosis-related genes*

The lipidomic analysis indicated an increase in the levels of polyunsaturated fatty acid (PUFA)-PC and a decrease in the levels of monounsaturated fatty acid (MUFA)-PC in the model groups,

which are consistent with the established metabolic profile of ferroptosis [17]. Further experimental validation was obtained to confirm the occurrence of ferroptosis in the model groups. Immunohistochemical (IHC) staining revealed the expression patterns of acyl-CoA synthetase long-chain family member 4 (*ACSL4*), lysophosphatidylcholine acyltransferase 3 (*LPCAT3*), and GSH peroxidase 4 (*GPX4*) in the sham and model groups (**Figure 6A-C**). In the model groups, the average optical density of *ACSL4* and *LPCAT3* was significantly higher and that of *GPX4* was significantly lower than those in the sham group (**Figure 6E**).

### *Biochemical indices of ferroptosis*

Compared with those in the sham group, we detected significant increases in the levels of ROS, Fe<sup>2+</sup>, and MDA in the 90 and 180 s model groups, whereas there was a significant decrease in the level of GSH (**Figure 6D**).

### *qRT-PCR analysis of key ferroptosis-associated genes*

The expression of *ACSL4*, *LPCAT3*, and *GPX4* was quantified using qRT-PCR. Consistent with the IHC results, compared with the expression levels in the sham group, there were significant increases in the expression of *ACSL4* and *LPCAT3* and a significant decrease in the expression of *GPX4* in the model groups (**Figure 6F**).

## Discussion

In this study, we examined the injury depth and pathological changes induced by exposure to NaOH. Macroscopically, the skin of rats in the 90 and 180 s model groups exhibited characteristics of second- and third-degree burns, respectively. Changes in fat-related skin structures, such as sebaceous gland epithelial lysis, an increase in the number of subcutaneous fat vacuoles, and loss of the serrated appearance of the fat layer, were observed in both groups. These findings indirectly support the hypothesis that alkaline substances saponify lipids, thereby rendering them more corrosive than acidic substances, and suggest that NaOH disrupts lipid metabolism in skin tissues, thereby enhancing its damaging effects.

The lipid components in organisms, including phospholipids (PLs), glycerides, sphingolipids,

and sterols [18], play essential roles in maintaining normal physiological activities via their synthesis and degradation, and the dysregulation of lipid metabolism can lead to the development of various diseases [19]. Our lipidomics results revealed elevated levels of PUFA-PLs, including PC (16:0e\_18:2), PC (18:0\_18:2), and PC (16:0e\_20:4), and reduced levels of MUFA-PLs, including PC (16:0\_16:1) and PC (16:1\_16:1), in the model group rats, consistent with the metabolic characteristics of ferroptosis [17].

Typically, MUFA-PCs confer cell membrane rigidity, whereas PUFA-PCs enhance membrane flexibility [20, 21]. However, although elevated PUFA-PC levels can contribute to enhancing cell fluidity and function, they are highly susceptible to oxidation and peroxidation owing to their polyunsaturated structure with multiple double bonds [17, 22]. Thus, elevated PUFA-PC levels can heighten the intrinsic risk of ferroptosis. Conversely, MUFA-PCs, which have fewer double bonds, tend to be more resistant to peroxidation and can competitively inhibit the proferroptotic effects of PUFAs, thereby acting as protective factors against ferroptosis [11]. Notably, unmodified free PUFAs do not drive ferroptosis, which occurs only when these PUFAs are esterified with PLs. Thus, ferroptotic lipid metabolism involves PUFA-PL synthesis, during which PUFAs are initially acylated by *ACSL4* to form PUFA-CoA [23, 24] and are then esterified by *LPCAT3* to form PUFA-PLs, which can participate in chain oxidation reactions [25, 26].

Physiologically, the body employs several mechanisms to counteract ferroptosis, with the *GPX4* system being the most notable [27]. *GPX4*, a downstream reductase of the x<sub>c</sub><sup>-</sup> system, uses its cofactor GSH to reduce peroxidised lipid components to form more stable hydroxyl lipids, thereby protecting against ferroptosis [28, 29]. Thus, inhibiting *GPX4* activity or expression can induce ferroptosis.

Iron, an essential trace element for biological activity, requires complex and efficient homeostatic regulation [30]. An imbalance in iron metabolism can also lead to the development of various diseases [31, 32]. Intracellular Fe<sup>2+</sup> can react with hydrogen peroxide to produce ROS via the Fenton reaction [33], and therefore, iron overload serves as a hallmark of ferroptosis

## Altered lipid metabolism in NaOH-induced skin burns

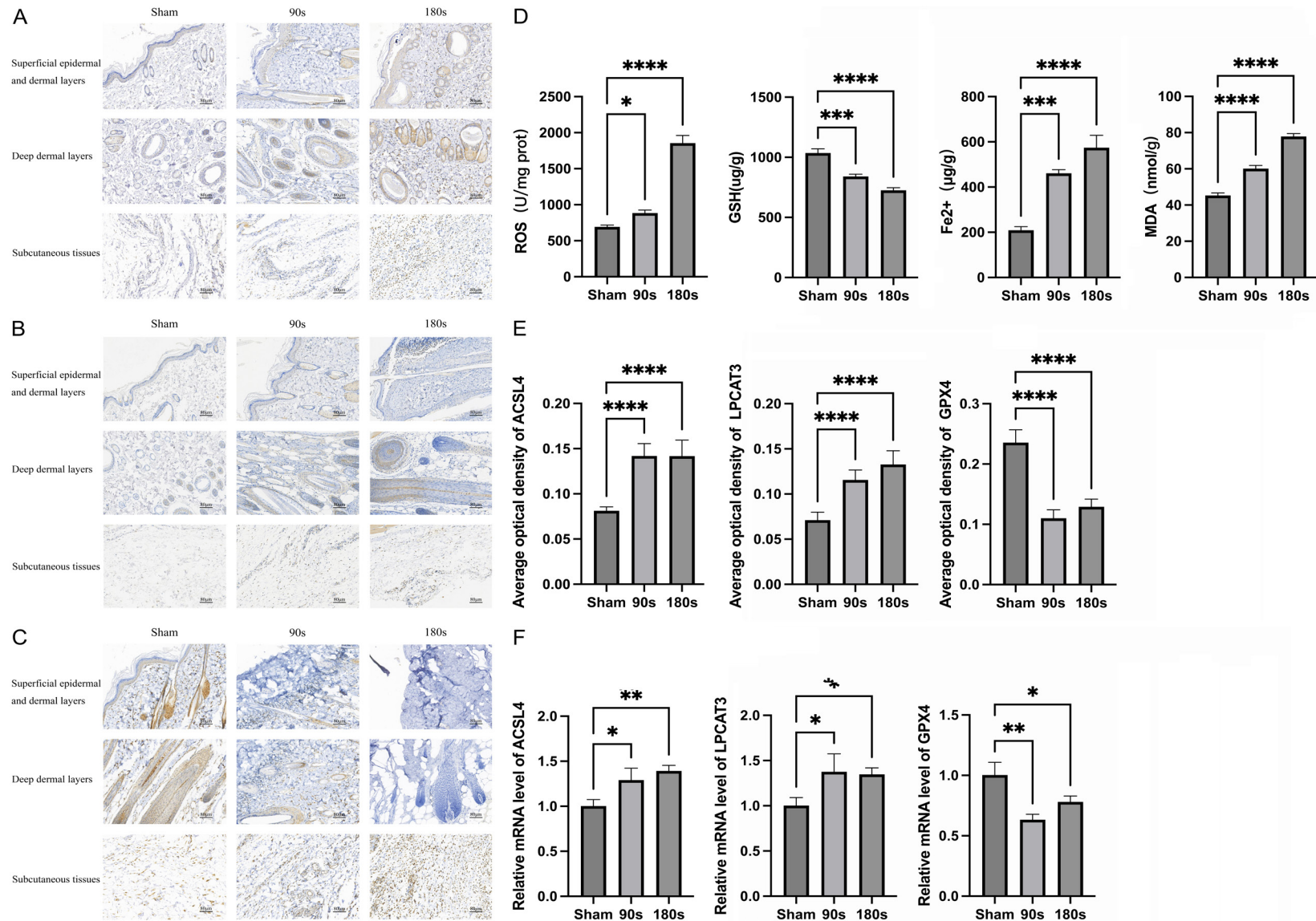


**Figure 6.** Ferroptosis in NaOH-induced burn wounds. (A-C) Immunohistochemical staining of (A) acyl-CoA synthetase long-chain family member 4 (ACSL4), (B) lysophosphatidylcholine acyltransferase 3 (LPCAT3), and (C) glutathione peroxidase 4 (GPX4) in each group (magnification  $\times 200$ ). (D) Comparison of reactive oxygen species, Fe<sup>2+</sup>, glutathione, and malondialdehyde content among the groups. (E) Average optical density levels of ACSL4, LPCAT3, and GPX4 in each group. (F) Messenger RNA expression levels of ACSL4, LPCAT3, and GPX4 in each group.

[25]. ROS are the reduced products of oxygen molecules, and play contrasting roles in oxidative stress and cell cycle regulation [34, 35]. ROS can directly damage phosphoribose backbones, leading to cell death, or act on the double bonds of DNA bases, causing ring-opening reactions and potential base mismatches, resulting in erroneous protein synthesis [36].

By virtue of its thiol structure, GSH can counter ROS toxicity by undergoing oxidation to glutathione disulfide. During this process, it provides electrons that can neutralise peroxides and functions in tandem with superoxide dismutase to exert antioxidant effects [37]. GSH deficiency or dysfunction can lead to the accumulation of ROS, which can attack molecules with double carbon bonds, causing oxidation and peroxidation. PUFAs are particularly susceptible—a process referred to as lipid peroxidation [38]. MDA, an end-product of lipid peroxidation that is often used as a biomarker of oxidative stress, can bind to biomolecules to form new epitopes with different biological and immunogenic properties [39].

In this study, we measured the levels of  $Fe^{2+}$ , ROS, GSH, and MDA in the skin tissues of experimental rats. The model group rats were characterised by significantly higher levels of  $Fe^{2+}$ , ROS, and MDA and significantly lower levels of GSH than the sham-treated rats, thereby providing evidence of substantial peroxidative damage and the occurrence of ferroptosis in NaOH-induced skin wounds. Based on these observations, we assessed the expression of key ferroptosis-related genes, namely *ACSL4*, *LPCAT3*, and *GPX4*.

IHC staining for *ACSL4* and *LPCAT3* revealed larger and deeper brownish-yellow areas in the superficial and deep dermis and subcutaneous tissue obtained from rats in the model groups, indicating the increased expression of these genes compared with that in the sham group. Furthermore, qRT-PCR analysis enabled us to confirm significant increases in the expression of these markers in the model rats, thus providing evidence of enhanced PUFA-PL synthesis in NaOH-induced skin wounds. In contrast, staining for *GPX4* revealed smaller, lighter brown-yellow areas in the epidermis and dermis of the skin tissues of the model rats. Consistently, qRT-PCR analysis revealed significantly lower *GPX4* expression in the model rats than in the

control rats, indicating insufficient antioxidant capacity. Collectively, these results indicate that NaOH induces ferroptosis in skin wounds by promoting the accumulation of lipid peroxides and inhibiting *GPX4* activity.

This study has certain limitations. First, IHC staining revealed an increase in the expression of *GPX4* in inflammatory cells within the subcutaneous tissue of both model groups, suggesting that inflammatory cells play a pivotal role in NaOH-induced skin damage, which warrants further investigation. Second, the experimental validation in this study was primarily performed at the tissue and organ levels, and sample sizes were limited owing to insufficient research funding. Accordingly, further research at the cellular level, using larger samples, is needed to elucidate the mechanisms underlying ferroptosis in the context of NaOH burns and to identify potential therapeutic strategies.

### Conclusions

In conclusion, we assessed the depth and pathological changes in NaOH-induced skin burns through morphological observations. Lipidomic analysis revealed a metabolic profile consistent with that of ferroptosis. Subsequent evaluations of oxidative stress, lipid peroxidation, iron metabolism, and key ferroptosis gene expression confirmed the disturbance of lipid metabolism and the occurrence of ferroptosis in NaOH-induced skin wounds.

### Acknowledgements

This research did not receive any specific grant from funding agencies in the public, commercial, or not-for-profit sectors.

### Disclosure of conflict of interest

None.

### Abbreviations

NaOH, sodium hydroxide; GSH, glutathione; SD, Sprague-Dawley; MS, mass spectrometry; m/z, mass-to-charge ratio; Rt, retention time; VIP, variable importance in projection; ROS, reactive oxygen species;  $Fe^{2+}$ , ferrous ion; MDA, malondialdehyde; qRT-PCR, quantitative reverse transcription-polymerase chain reaction; UH-PLC-QTOF/MS, ultra-high-performance liquid chromatography coupled with quadrupole time-

of-flight mass spectrometry; SM, sphingomyelin; phSM, phytosphingosine; PG, phosphatidylglycerol; PE, phosphatidylethanolamine; PC, phosphatidylcholine; LPC, lysophosphatidylcholine; CerP, ceramide phosphate; Cer, ceramide; LPG, lysophosphatidylglycerol; Hex2Cer, dihexosylceramide; PUFA, polyunsaturated fatty acid; MUFA, monounsaturated fatty acid; IHC, immunohistochemical; ACSL4, acyl-CoA synthetase long-chain family member 4; LPCAT3, lysophosphatidylcholine acyltransferase 3; GPX4, GSH peroxidase 4; PL, phospholipid.

**Address correspondence to:** Dan Xu, The Third Xiangya Hospital of Central South University, No. 138, Tongzipo Road, Yuelu District, Changsha 410013, Hunan, China. E-mail: 44654266@qq.com

### References

- [1] Abbasi H, Dehghani A, Mohammadi AA, Ghadimi T and Keshavarzi A. The epidemiology of chemical burns among the patients referred to burn centers in Shiraz, Southern Iran, 2008-2018. *Bull Emerg Trauma* 2021; 9: 195-200.
- [2] Chai H, Chaudhari N, Kornhaber R, Cuttle L, Fear M, Wood F and Martin L. Chemical burn to the skin: a systematic review of first aid impacts on clinical outcomes. *Burns* 2022; 48: 1527-43.
- [3] Said DG and Dua HS. Chemical burns acid or alkali, what's the difference? *Eye (Lond)* 2020; 34: 1299-300.
- [4] Greenwood JE, Tan JL, Ming JC and Abell AD. Alkalis and skin. *J Burn Care Res* 2016; 37: 135-41.
- [5] Ko CW, Qu J, Black DD and Tso P. Regulation of intestinal lipid metabolism: current concepts and relevance to disease. *Nat Rev Gastroenterol Hepatol* 2020; 17: 169-83.
- [6] Yin X, Xu R, Song J, Ruze R, Chen Y, Wang C and Xu Q. Lipid metabolism in pancreatic cancer: emerging roles and potential targets. *Cancer Commun (Lond)* 2022; 42: 1234-56.
- [7] Han X and Gross RW. The foundations and development of lipidomics. *J Lipid Res* 2022; 63: 100164.
- [8] Wu Z, Bagarolo GI, Thorøe-Boveleth S and Jankowski J. "Lipidomics": mass spectrometric and chemometric analyses of lipids. *Adv Drug Deliv Rev* 2020; 159: 294-307.
- [9] Dixon SJ, Lemberg KM, Lamprecht MR, Skouta R, Zaitsev EM, Gleason CE, Patel DN, Bauer AJ, Cantley AM, Yang WS, Morrison B 3<sup>rd</sup> and Stockwell BR. Ferroptosis: an iron-dependent form of nonapoptotic cell death. *Cell* 2012; 149: 1060-72.
- [10] Zeng F, Nijiati S, Tang L, Ye J, Zhou Z and Chen X. Ferroptosis detection: from approaches to applications. *Angew Chem Int Ed Engl* 2023; 62: e202300379.
- [11] Pope LE and Dixon SJ. Regulation of ferroptosis by lipid metabolism. *Trends Cell Biol* 2023; 33: 1077-87.
- [12] Yang WS and Stockwell BR. Ferroptosis: death by lipid peroxidation. *Trends Cell Biol* 2016; 26: 165-76.
- [13] Chen X, Kang R, Kroemer G and Tang D. Broadening horizons: the role of ferroptosis in cancer. *Nat Rev Clin Oncol* 2021; 18: 280-96.
- [14] Jaspers MEH, van Haasterecht L, van Zuijlen PPM and Mokkink LB. A systematic review on the quality of measurement techniques for the assessment of burn wound depth or healing potential. *Burns* 2019; 45: 261-81.
- [15] Akelma H and Karahan ZA. Rare chemical burns: review of the literature. *Int Wound J* 2019; 16: 1330-8.
- [16] Livak KJ and Schmittgen TD. Analysis of relative gene expression data using real-time quantitative PCR and the 2- $\Delta\Delta$ CT method. *Methods* 2001; 25: 402-8.
- [17] Mortensen MS, Ruiz J and Watts JL. Polyunsaturated fatty acids drive lipid peroxidation during ferroptosis. *Cells* 2023; 12: 804.
- [18] Wymann MP and Schneider R. Lipid signalling in disease. *Nat Rev Mol Cell Biol* 2008; 9: 162-76.
- [19] Bian X, Liu R, Meng Y, Xing D, Xu D and Lu Z. Lipid metabolism and cancer. *J Exp Med* 2021; 218: e20201606.
- [20] Han X, Yang J, Yang K, Zhao Z, Abendschein DR and Gross RW. Alterations in myocardial cardiolipin content and composition occur at the very earliest stages of diabetes: a shotgun lipidomics study. *Biochemistry* 2007; 46: 6417-28.
- [21] Ridgway ND. The role of phosphatidylcholine and choline metabolites to cell proliferation and survival. *Crit Rev Biochem Mol Biol* 2013; 48: 20-38.
- [22] Chen C, Li R and Wu H. Recent progress in the analysis of unsaturated fatty acids in biological samples by chemical derivatization-based chromatography-mass spectrometry methods. *J Chromatogr B Analyt Technol Biomed Life Sci* 2023; 1215: 123572.
- [23] Liang D, Minikes AM and Jiang X. Ferroptosis at the intersection of lipid metabolism and cellular signaling. *Mol Cell* 2022; 82: 2215-27.
- [24] Ding K, Liu C, Li L, Yang M, Jiang N, Luo S and Sun L. Acyl-CoA synthase ACSL4: an essential target in ferroptosis and fatty acid metabolism. *Chin Med J (Engl)* 2023; 136: 2521-37.
- [25] Tang D, Chen X, Kang R and Kroemer G. Ferroptosis: molecular mechanisms and health implications. *Cell Res* 2021; 31: 107-25.
- [26] Lagrost L and Masson D. The expanding role of lyso-phosphatidylcholine acyltransferase-3

## Altered lipid metabolism in NaOH-induced skin burns

- (LPCAT3), a phospholipid remodeling enzyme, in health and disease. *Curr Opin Lipidol* 2022; 33: 193-8.
- [27] Tian H, Niu H, Luo J, Yao W, Chen X, Wu J, Geng Y, Gao W, Lei A, Gao Z, Tian X, Zhao X, Shi H, Li C and Hua J. Knockout of stearoyl-CoA desaturase 1 decreased milk fat and unsaturated fatty acid contents of the goat model generated by CRISPR/Cas9. *J Agric Food Chem* 2022; 70: 4030-43.
- [28] Dalleau S, Baradat M, Guéraud F and Huc L. Cell death and diseases related to oxidative stress: 4-hydroxynonenal (HNE) in the balance. *Cell Death Differ* 2013; 20: 1615-30.
- [29] Liu J, Kang R and Tang D. Signaling pathways and defense mechanisms of ferroptosis. *FEBS J* 2022; 289: 7038-50.
- [30] Galy B, Conrad M and Muckenthaler M. Mechanisms controlling cellular and systemic iron homeostasis. *Nat Rev Mol Cell Biol* 2024; 25: 133-55.
- [31] Morales M and Xue X. Targeting iron metabolism in cancer therapy. *Theranostics* 2021; 11: 8412-29.
- [32] Abbasi U, Abbina S, Gill A, Takuechi LE and Kizhakkedathu JN. Role of iron in the molecular pathogenesis of diseases and therapeutic opportunities. *ACS Chem Biol* 2021; 16: 945-72.
- [33] Yoshida M, Minagawa S, Araya J, Sakamoto T, Hara H, Tsubouchi K, Hosaka Y, Ichikawa A, Saito N, Kadota T, Sato N, Kurita Y, Kobayashi K, Ito S, Utsumi H, Wakui H, Numata T, Kaneko Y, Mori S, Asano H, Yamashita M, Odaka M, Morikawa T, Nakayama K, Iwamoto T, Imai H and Kuwano K. Involvement of cigarette smoke-induced epithelial cell ferroptosis in COPD pathogenesis. *Nat Commun* 2019; 10: 3145.
- [34] Floros KV, Cai J, Jacob S, Kurupi R, Fairchild CK, Shende M, Coon CM, Powell KM, Belvin BR, Hu B, Puchalapalli M, Ramamoorthy S, Swift K, Lewis JP, Dozmorov MG, Glod J, Koblinski JE, Boikos SA and Faber AC. MYCN-amplified neuroblastoma is addicted to iron and vulnerable to inhibition of the system Xc-/glutathione axis. *Cancer Res* 2021; 81: 1896-908.
- [35] Sahoo BM, Banik BK, Borah P and Jain A. Reactive oxygen species (ROS): key components in cancer therapies. *Anticancer Agents Med Chem* 2022; 22: 215-22.
- [36] Friedmann Angeli JP, Schneider M, Proneth B, Tyurina YY, Tyurin VA, Hammond VJ, Herbach N, Aichler M, Walch A, Eggenhofer E, Basavarajappa D, Rådmark O, Kobayashi S, Seibt T, Beck H, Neff F, Esposito I, Wanke R, Förster H, Yefremova O, Heinrichmeyer M, Bornkamm GW, Geissler EK, Thomas SB, Stockwell BR, O'Donnell VB, Kagan VE, Schick JA and Conrad M. Inactivation of the ferroptosis regulator Gpx4 triggers acute renal failure in mice. *Nat Cell Biol* 2014; 16: 1180-91.
- [37] Fang X, Ardehali H, Min J and Wang F. The molecular and metabolic landscape of iron and ferroptosis in cardiovascular disease. *Nat Rev Cardiol* 2023; 20: 7-23.
- [38] Jiang M, Jike Y, Liu K, Gan F, Zhang K, Xie M, Zhang J, Chen C, Zou X, Jiang X, Dai Y, Chen W, Qiu Y and Bo Z. Exosome-mediated miR-144-3p promotes ferroptosis to inhibit osteosarcoma proliferation, migration, and invasion through regulating ZEB1. *Mol Cancer* 2023; 22: 113.
- [39] Dyall SC, Balas L, Bazan NG, Brenna JT, Chiang N, da Costa Souza F, Dalli J, Durand T, Galano JM, Lein PJ, Serhan CN and Taha AY. Polyunsaturated fatty acids and fatty acid-derived lipid mediators: recent advances in the understanding of their biosynthesis, structures, and functions. *Prog Lipid Res* 2022; 86: 101165.